

Date of publication xxxx 00, 0000, date of current version xxxx 00, 0000.

Digital Object Identifier xx.xxxx/ACCESS.2021.DOI

LaUV: A Physics-Based UV Light Simulator for Disinfection and Communication Applications

Maria S. Baltadourou¹, Konstantinos K. Delibasis¹, Georgios N. Tsigaridas², Harilaos G. Sandalidis¹, and George K. Karagiannidis³, (Fellow, IEEE)

¹Department of Computer Science and Biomedical Informatics, University of Thessaly, GR-35131 Lamia, Greece

²Department of Physics, School of Applied Mathematical and Physical Sciences, National Technical University of Athens, GR-15780 Zografou, Athens, Greece

³Department of Electrical and Computer Engineering, Aristotle University of Thessaloniki, GR-54124, Thessaloniki, Greece

Corresponding author: K.K. Delibasis(e-mail: kdelibasis@gmail.com).

ABSTRACT The sterilization properties of the C-band of the ultraviolet (UV) light have been well-known for many years; however, their application has become more vital and widespread today due to the Covid-19 pandemic. Nevertheless, minimal work has been devoted to simulating UV-C propagation for surface disinfection in indoor environments. UV light has also been proposed for non-line-of-sight (NLOS) outdoor communication applications, where a number of simulators have been developed, but with several simplifications. The current work presents a fully-featured simulator for UV light propagation, called LaUV, designed mainly for indoor settings, capable of calculating measurable parameters that can be used for indoor surface disinfection and communication applications. LaUV considers atmospheric absorption and scattering according to Rayleigh and Mie theory, and reflections from rough surfaces. The scattering cross-section and probability density function of the scattering angles (phase function) are calculated accurately for any wavelength, concentration, and diameter distribution of spherical scattering particles (aerosols and droplets). Examples are presented for indoor environments, including empty rooms and rooms with furniture, for different environmental conditions and surface albedos. Interesting initial conclusions can be drawn, considering the spatial distribution of UV exposure for surface disinfection applications and channel modeling for line-of-sight (LOS) and NLOS communication, demonstrating the versatility and the potential applications of the proposed simulator.

INDEX TERMS Ultraviolet (UV) light, Channel modeling, Monte Carlo simulation, Indoor communications, Surface disinfection

I. INTRODUCTION

ULTRAVIOLET (UV) light, especially in the C band (UV-C), exhibits sterilization properties against bacteria, viruses, and fungi, already known for many years. The research interest for these properties has been revived due to current coronavirus epidemiological conditions [1]. Furthermore, UV-C light has also been considered for non-line-of-sight (NLOS) outdoor communication applications for distances of a few hundred meters due to its increased bandwidth [2]. Last but not least, it needs emphasizing that some recent studies recommend UV-C for indoor communication applications as an effective alternative means of other optical technologies [3]. Based on the above, it becomes evident

that the exploitation of UV radiation for health purposes and communication will intensify even more in the coming years. Therefore, computational tools that simulate accurately the physical phenomena that take place during light propagation in appropriate experimental settings, are expected to gain importance.

A. RELATED WORK

The application of UV-C spectrum in outdoor communications dates back to the previous decades, and Monte Carlo (MC) methods were applied to model the corresponding channel characteristics (see [4] and the references therein). In summary, some typical studies are as follows. First, an

MC simulation for an NLOS outdoor channel with atmospheric scattering phenomena was described in [5], and several atmospheric conditions were considered for a range of wavelengths. Second, in [6], a method was introduced to model the impulse response of an NLOS outdoor UV communication channel with Rayleigh and Mie scattering. However, the scattering angle probability was approximated using the generalized Henyey-Greenstein (HG) function instead of the accurate Mie calculations. In particular, when scattering depends intensely on particle diameters, that approximation may cause inaccuracies. Results were presented for many wavelengths spanning the UV-C spectrum for a single atmospheric conditions scenario. Then, in [7], the MC method, combined with point probability, was applied to simulate a UV atmospheric communication model. Nevertheless, the Mie scattering angle probability was expressed with the HG phase function having a single set of parameters, thus, not allowing for accurate results for different air conditions. Finally, the authors in [8] adopted the HG phase function approximation to study the effect of aerosols on the ground point spread function of high altitude light sources.

Some individual studies have lately emerged dealing with the possibility of applying UV as an alternative means for providing diffuse optical communications in indoor environments. The general framework on the design and implementation of some systems is adequately described in [3]. In [9], a novel dynamic beamforming method has been suggested which makes use of the distance to estimate the user location. Note that the challenges of an indoor optical wireless medical body area network were discussed in [10], where the MC method was employed to estimate the channel impulse response (CIR). A simple model of an empty room was considered, while a 3D model of a person was allowed to move in random trajectories. Best fit statistical models to describe the distribution of these parameters for more general scenarios were proposed.

The germicidal properties of UV-C light have been explored as a function of wavelength for different viruses, bacteria, and fungi, for a long. Theoretical and experimental findings revealed a strong germicidal effect of UV-C light between 200 and 280 nm, with an intermediate peak at 254 nm [11]. A pretty recent study indicated that the far UV-C light (207-222 nm) efficiently kills pathogens such as human coronaviruses and influenza [1], potentially without harm to exposed human tissues [12]. Several reports focused on coronavirus surface disinfection with encouraging experimental results [1], [13] but they only treat the issues of exposure measurements and biological effectiveness. Furthermore, a review of viruses and bacteria deactivation using UV-C light at different wavelengths (mainly 222 and 254 nm) was discussed in [14].

The application of UV-C light to air disinfection, especially in medical facilities, has also been investigated, both for upper-room air exposure combined with natural air convection or in-ducts air exposure [15]. Somewhat less attention has been given to surface exposure. For instance, in [16],

[17], experimental measurements were reported with a mobile UV-C generator in a hospital room. Limited approaches to surface disinfection simulation were presented in [18] and most recently in [19] with applications to coronavirus but without considering the physics of UV atmospheric propagation. In the work of [20], a 3×3 UV-C LED array was designed to disinfect small packaging, and its effectiveness was assessed with a simple ray-tracing simulator.

Few relevant works appeared trying to utilize a free illumination design software package [21]. In [22], the DIALux software was employed to simulate the UV dose distribution on respirator masks in a small disinfection chamber. Very recently, an attempt to assess the utilization of DIALux for UV light was reported in [23], in comparison to the commercial software OpticStudio used to design optical instruments [24]. DIALux is essentially a ray-tracer producing photorealistic renderings for many materials and commercial light sources, which currently allows incorporating UV light sources. However, the accurate physics of UV light propagation was not studied either in DIALux or OpticStudio. The atmospheric scattering appears to be ignored in both software packages, as verified in [23, (Fig. 4)], whereas the term *scattering* is used to model reflection from rough surfaces. The effect of temperature, air humidity, and droplet/aerosol size distribution is also not included in these software packages.

B. MOTIVATION AND CONTRIBUTION

A physics-based MC simulator of UV light propagation in an indoor environment, named LaUV, is proposed in the present work¹. The simulated indoor scene may be closed, where photons cannot escape the scene but may be attenuated during their interaction with surfaces, or open, where photons may leave the scene from openings with no triangulation, such as doors or windows. The simulator can handle any number of objects in the scene with arbitrary geometry, provided they have been triangulated. It considers atmospheric scattering in a very accurate manner and reflection from rough surfaces. Furthermore, scattering from spherical water droplets and aerosols is explicitly handled. In contrast, most UV propagation simulators approximate the Rayleigh and the Mie scattering angle using the HG or the more general Gegenbauer-Kernel function (GK) phase function. These convenient approximations allow for faster generation of random scattering angles, and even if they can be parameterized, their accuracy is limited, affecting the overall accuracy of the simulation [25], [26]. In [27], the utilization of the Mie phase function was found to be more accurate than the HG, or GK function, according to experimental results for blood scattering.

A case of photon propagation, well-studied in the literature, considers semi-infinite continuous absorbing media that include small regions of specific shapes with different optical properties, such as layered tissues containing spheres

¹The acronym *LaUV* comes from the combination of the word *Lamia*, the Greek city that is the place of origin, living, or working of most of the authors of the paper, and the word *ultraviolet*.

or slabs. In those settings, MC variations, such as the perturbation method (pMC) and the scaling method (sMC) have been introduced [28] to alleviate the problem of the high computational burden. These variations utilize one or few traditional MC executions and attempt to predict the MC outcome in slightly different settings, such as small displacements of the source or changes in the optical properties of the absorbing media in small regions. However, the problem of simulating photon propagation in indoor environments with complicated triangulated surfaces, e.g., furniture, is very different from the problems mentioned above, and no such attempt to use pMC or sMC have been reported to our knowledge. Well-established approaches that apply MC to media with triangulated surface interface also utilize the traditional MC with specific calculation optimizations. For instance, in [29] the proposed triangular mesh-based MC (MMCM) utilizes ray tracing with Pluecker coordinates to solve the ray-triangle intersection problem, although using approximating phase functions. A similar approach is followed in [26]. TIMOS [30], an MC applied to tetrahedra, also uses traditional MC with ray tracing that intersects the four faces of the tetrahedron inside which the photon is propagating. None of these approaches propose the use of pMC, sMC or similar techniques.

The proposed work implements the physics of photon propagation and scattering, simulating the physical phenomena at the level of photons. Other approaches perform the simulation considering packets of photons [31]. Although such approaches may improve the statistics, several assumptions and simplifications are usually required, which deteriorate accuracy. For instance, in [31], the scattering angle is not estimated accurately for each different size of nanoparticles; instead, it is calculated using an approximating phase function, typical for all scattering events, whereas absorption is also handled using a heuristic rule at the packet level. Although packet handling may be advantageous for light propagation in absorbing media, such as tissue, it does not appear to offer any advantages in simulating the propagation in the atmosphere that considers scattering with different size nanoparticles without significant absorption. Thus, the approach of simulation of individual photon propagation with an accurate description of the physical phenomena was selected in our work.

The measurable outputs are designed for UV-C-based surface disinfection, as well as indoor and outdoor optical communication applications. The overall contribution of the work can be summarized on the following topics:

- Atmospheric scattering is simulated accurately by calculating the cross-section and scattering angle probability distribution directly from the Rayleigh and Mie theory for spherical nanoparticles, without resorting to approximating phase functions.
- The air humidity and temperature are also considered, and accurate droplet and aerosol diameter distributions are used to simulate different atmospheric conditions scenarios, occurring naturally or artificially with nebu-

lizers.

- The simulator provides the following results per elementary surface triangle: the UV exposure as implicitly indicated by the number of photons absorbed per surface unit area, the contribution of each phenomenon to exposure, and the distribution of the total path length of absorbed photons.
- The calculations mentioned above can accurately be performed for any wavelength, λ , thus allowing experimentation with any λ values, such as 207, 222, and 254 nm, which reportedly have biological significance both for humans and viruses/bacteria/fungi [1], [11]–[13].
- These measurements can be used to calculate the disinfection fraction for any geometric setup of light sources and indoor objects and model the extinction rate for any given point of the indoor environment.
- Finally, the mean of the total path length of each photon absorbed in any triangle can easily be converted to the channel impulse response between the source and this triangle, thus completing the channel modeling process.

C. STRUCTURE

The rest of the paper is organized as follows. Section II briefly discusses the physics of light propagation in the air in the presence of spherical aerosols and droplets, with particular references to Rayleigh and Mie scattering and photon absorption phenomena. Section III describes the overall methodology to implement the single-photon propagation and scattering and reflection phenomena in any indoor environment after triangulating the existing objects. Section IV describes the simulation scenarios used to present several measurable quantities for three different atmospheric conditions and two surface albedo values A , assuming an empty room and a room with furniture. Finally, some helpful concluding remarks are drawn in Section V with a brief discussion regarding the applicability of LaUV to optical communications and surface disinfection.

II. PHYSICS OF LIGHT PROPAGATION

When radiation interacts with air molecules and other aerosol/droplets, scattering and absorption phenomena occur. The cross-section and scattering angle distributions adopted in the current study are described below.

A. RAYLEIGH SCATTERING

For particles with diameter, d , up to 10 times smaller than the incident photon wavelength, λ , the scattering process is described by the Rayleigh theory. The cross-section for an airborne particle with refractive index, n , is derived by [32, eq. (1)]

$$\sigma_R = \frac{2\pi^5}{3} \frac{d^6}{\lambda^4} \left(\frac{n^2 - 1}{n^2 + 2} \right)^2. \quad (1)$$

The distribution of radiation with respect to the scattering angle θ is expressed by [33]

$$\frac{I(\theta)}{I_0} = \frac{1 + \cos^2\theta}{2}, \quad (2)$$

which applies to random polarization and is independent of λ and d . According to (1), the Rayleigh scattering cross-section for dry air is proportional to λ^{-4} and is obtained by

$$\sigma_{sR, dry} = \sigma_0 \lambda^{-4}, \quad (3)$$

where $\sigma_0 \approx 4.4 \times 10^{-16} \text{ cm}^2 \text{ nm}^{-4}$.

Roughly speaking, the atmosphere is a mixture of dry air and water particles. The water vapor density, ρ_ν , can be calculated based on [34]

$$\rho_\nu = R_H \rho_{s\nu}, \quad (4)$$

where R_H is the relative humidity and $\rho_{s\nu}$ is the saturated vapor density. It was shown that for values of temperature T up to 40°C (degrees Celsius), is estimated as [34]

$$\rho_{s\nu} = \tau_0 + \tau_1 T + 8.1847 \times 10^{-3} T^2 + 3.1243 \times 10^{-4} T^3, \quad (5)$$

where $\tau_0 = 5.018$, and $\tau_1 = 0.32321$. Typical values for ρ_ν are in the range of a few $\text{g} \cdot \text{m}^{-3}$. It needs mentioning that the diameter of a single water molecule is approximately equal to 0.28 nm [35]; however, the water exists in the air in the form of moisture particles with a diameter ranging from 1 nm to a few μm much larger than the molecular diameter [36]. In general, the concentration of water particles of diameter, d , smaller than λ , i.e., the number of particles present in unit volume, is expressed by

$$\rho_N = \frac{\rho_\nu}{\rho_w \frac{1}{6} \pi d^3}, \quad (6)$$

where ρ_w is the water density. Assuming that all the water particles in the air have the same diameter, the Rayleigh scattering coefficient μ_{sR} (also known as extinction coefficient measured in m^{-1}) is specified as

$$\mu_{sR} = \sigma_{sR, dry} \rho_{N, dry} + \sigma_w \rho_N, \quad (7)$$

where σ_w is calculated for any λ according to (1), n is obtained from [37] at the selected wavelength and $\rho_{N, dry}$ is the concentration of scatterers in dry air (number per m^3). The mean free path of each photon for Rayleigh scattering is readily obtained as

$$\bar{l}_{fR} = \frac{1}{\mu_{sR}}, \quad (8)$$

Further, the mean free path, l_f , is related to the atmospheric visibility by the Koschmieder equation [38]

$$l_V = \frac{3.912}{\mu_{sR}} = 3.912 \bar{l}_{fR}. \quad (9)$$

By assuming particles with uniform diameter and combining (4)-(9), we can easily estimate the water particle diameter as a function of

$$d = \frac{2.584 \times 10^{-8}}{[l_V R_H \rho_{s\nu}]^{1/3}}. \quad (10)$$

For example, assuming that $T = 25^\circ\text{C}$, $R_H = 50\%$, and $l_V = 10 \text{ km}$, (9) implies that the diameter of water droplets corresponding to this environmental condition is $d = 5.307 \text{ nm}$. It becomes evident that during average atmospheric visibility, the diameter of water particles is much smaller than the wavelength, justifying the assumption that the interaction between the photons and the water droplets can adequately be described by Rayleigh scattering.

Figure 1 illustrates the values of μ_{sR} , calculated as described above, for $T = 20^\circ\text{C}$, $R_H = 50\%$, and λ between 200 nm and 300 nm, for four different particle diameters: 0.275, 1, 2, and 5 nm. As it can be observed, the value of μ_{sR} due to Rayleigh scattering is very low; thus, the mean free path for a photon with $\lambda = 200 \text{ nm}$ takes values from 50 m (for water particle diameter equal to 5 nm) to more than 1000 m (for single water molecules). In practice, under normal atmospheric conditions, the values of μ_{sR} usually lie in the range $10^{-2} - 10^{-1} \text{ m}^{-1}$, resulting in a mean free path between 10 and 100 m. Thus, Rayleigh scattering has a negligible effect on the indoor propagation of UV radiation, even for high relative humidity. Furthermore, since the value of the atmospheric absorption coefficient, $\mu_{\alpha R}$, is two to three orders of magnitude lower than μ_{sR} , it is practically negligible in indoor environments [39].

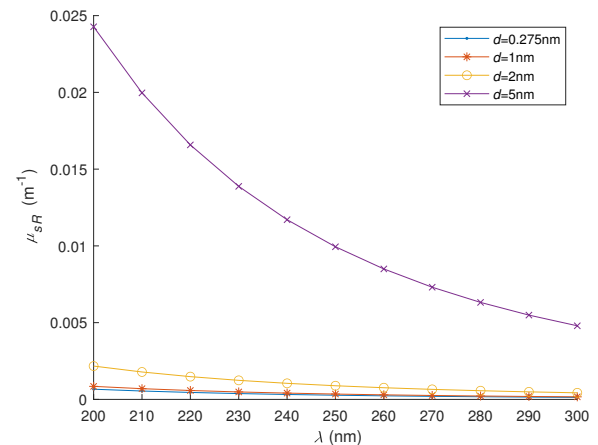


FIGURE 1. Rayleigh scattering coefficient vs. wavelength for $T = 20^\circ\text{C}$ and $R_H = 50\%$.

B. MIE SCATTERING FOR SPHERICAL NANOPARTICLES

The Mie scattering theory applies to particles with a diameter comparable to or greater than λ . It is necessary to include Mie scattering in LaUV since the concentration of water particles in the air and the distribution of their size varies with the meteorological conditions and human activity, e.g., pollution. Furthermore, artificially induced humidity using nebulizers produces water particles with a diameter between 500 and 5000 nm [40]. In these cases, the predictions of the Rayleigh theory for μ_{sR} will not be accurate. On the other hand, the Mie theory is accurate for scattering particles with a diameter of λ or larger and smaller particles, reproducing the Rayleigh

results in the latter case. Thus, Rayleigh scattering can be considered a particular case of Mie scattering.

According to Mie theory [31], [41], the extinction, scattering, and backscattering efficiency of a spherical nanoparticle, namely the ratio of the extinction, scattering, and backscattering cross-sections to the geometrical cross-section of the particle, respectively are expressed according to the formulae

$$Q_{ext} = \frac{2}{\zeta^2} \sum_{n=1}^{\infty} (2n+1) \operatorname{Re}(a_n + b_n), \quad (11)$$

$$Q_{scat} = \frac{2}{\zeta^2} \sum_{n=1}^{\infty} (2n+1) (|a_n|^2 + |b_n|^2), \quad (12)$$

$$Q_{back} = \frac{1}{4\pi\zeta^2} \left| \sum_{n=1}^{\infty} (2n+1) (-1)^n (a_n - b_n) \right|^2. \quad (13)$$

where

$$a_n = \frac{\psi_n(\zeta) \psi'_n(m\zeta) - m\psi'_n(\zeta) \psi_n(m\zeta)}{\xi_n(\zeta) \psi'_n(m\zeta) - m\xi'_n(\zeta) \psi_n(m\zeta)}, \quad (14)$$

$$b_n = \frac{m\psi_n(\zeta) \psi'_n(m\zeta) - \psi'_n(\zeta) \psi_n(m\zeta)}{m\xi_n(\zeta) \psi'_n(m\zeta) - \xi'_n(\zeta) \psi_n(m\zeta)}.$$

Here, $m = n/n_m$ and $\zeta = kR$, where n and n_m are the complex refractive indices of the particle and the surrounding medium respectively, R is the particle radius, and $k = 2\pi n_m/\lambda$ is the wavenumber in the surrounding medium. The functions $\psi_n(\zeta)$ and $\xi_n(\zeta)$ are the spherical Bessel and spherical Hankel functions, respectively, defined in [42, eq. (10.1.1)]. The prime denotes differentiation with respect to the argument. The absorption efficiency is obtained by the difference

$$Q_{abs} = Q_{ext} - Q_{scat} = \frac{2}{\zeta^2} \sum_{n=1}^{\infty} (2n+1) \left[\operatorname{Re}(a_n + b_n) - |a_n|^2 - |b_n|^2 \right]. \quad (15)$$

Equations (11) and (12) are obtained by integrating the Poynting vectors corresponding to the incident and scattered fields on the surface of a sphere concentric to the particle [31], [41]. Of note, these results are independent of the hypothetical integration sphere radius, and thus they are valid both for the near-field and the far-field zone. Since the absorption cross-section of the water particles at the desired wavelengths (200-300 nm) is two to three orders of magnitude lower than the scattering cross-section, the extinction coefficient can be considered equal to the scattering coefficient (measured in m^{-1}), given by the formula

$$\mu_{sM} = \rho_N \sigma_{sM} = \rho_N Q_{scat} \pi \frac{d^2}{4}, \quad (16)$$

where σ_{sM} is the Mie scattering cross-section. Figure 2 illustrates σ_{sM} as a function of λ and d for relative humidity 80% and temperature 20°C.

Furthermore, the angular distributions of the scattered radiation intensity for light polarized perpendicular and parallel

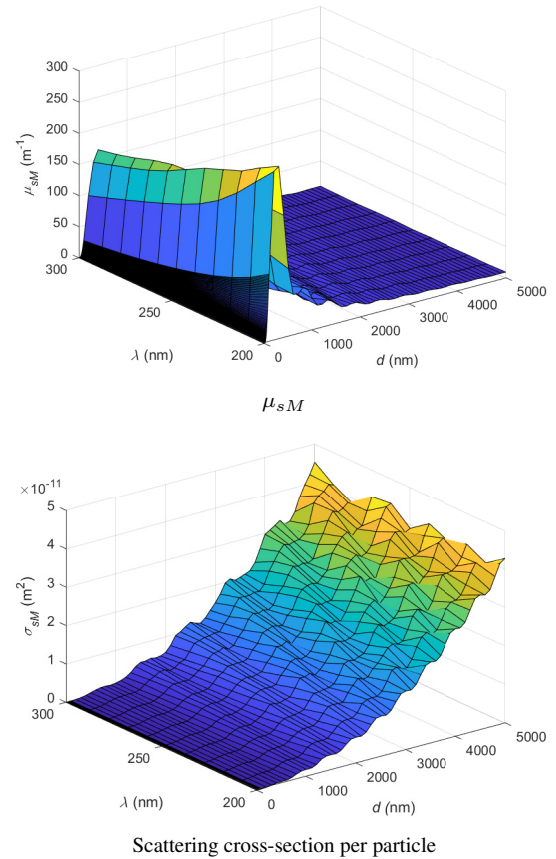


FIGURE 2. The Mie scattering coefficient and scattering cross-section per particle as a function of λ and d for $R_H = 80\%$ and $T = 20^\circ C$.

to the plane defined by the incident and scattered photons (scattering plane) are expressed by [31, eqs. (5.30-31)]

$$I_{\perp}(\theta) = \left| \sum_{n=1}^{\infty} \frac{2n+1}{n(n+1)} [a_n \kappa_n(\theta) + b_n \tau_n(\theta)] \right|^2, \quad (17)$$

and

$$I_{\parallel}(\theta) = \left| \sum_{n=1}^{\infty} \frac{2n+1}{n(n+1)} [a_n \tau_n(\theta) + b_n \kappa_n(\theta)] \right|^2, \quad (18)$$

where $\tau_n(\theta) = \frac{d}{d\theta} P_{n1}(\cos\theta)$ and $\kappa_n(\theta) = \frac{P_{n1}(\cos\theta)}{\sin\theta}$, with $P_{n1}(\cos\theta)$ being the associated Legendre polynomials for $m = 1$ [42, ch. 8]. Consequently, the probability of a photon scattered at an angle θ regarding the incident direction is proportional to $I_{\perp}(\theta)$ and $I_{\parallel}(\theta)$ for light polarized perpendicular and parallel to the scattering plane, respectively. For non-polarized light, the probability for a photon scattered at an angle θ can be considered proportional to

$$p(\theta) \simeq \frac{I_{\parallel}(\theta) + I_{\perp}(\theta)}{2} \quad (19)$$

Figure 3 depicts the probability of Mie scattering at different angles in polar coordinates for several combinations of the wavelength and particle diameter. It appears evident that as the particle diameter increases, the probability of

scattering at small angles (relative to the direction of the incident radiation) also gets high.

C. SPHERICAL PARTICLES WITH DIFFERENT DIAMETERS

In any realistic scenario, the atmospheric humidity consists of spherical water particles with different diameters. The concentration of water particles as a function of their diameter is based on the modified gamma distribution [36, eq. (1)]

$$\rho(d) = n_0 \left(\frac{d}{2}\right)^\alpha \exp\left[-\frac{\alpha}{\gamma} \left(\frac{d}{d_0}\right)^\gamma\right], \quad (20)$$

where n_0 is the total number of particles, α is a positive integer, γ is a positive real number, and d_0 is the particle diameter at maximum frequency. The values of these parameters for different atmospheric conditions can be found in the literature.

The probability, π_i , for the particle with diameter d_i is estimated according to (20), setting $n_0 = 1$ [43]. Furthermore, the concentration of every particle, ρ_i , is derived through the following linear system

$$\mathbf{M}\boldsymbol{\rho} = \mathbf{B}, \quad (21)$$

$$\text{where } \mathbf{M} = \begin{pmatrix} \delta m_1 & \delta m_2 & \delta m_3 & \cdots & \delta m_N \\ \pi_2 & -\pi_1 & 0 & \cdots & 0 \\ \pi_3 & 0 & -\pi_1 & \cdots & 0 \\ \vdots & \vdots & \vdots & \ddots & 0 \\ \pi_N & 0 & 0 & \cdots & -\pi_1 \end{pmatrix},$$

$$\boldsymbol{\rho} = \begin{pmatrix} \rho_1 \\ \rho_2 \\ \rho_3 \\ \vdots \\ \rho_N \end{pmatrix}, \quad \mathbf{B} = (\varrho_\nu \quad 0 \quad \dots \quad 0)^T, \quad \varrho_\nu \text{ expresses the}$$

total mass of water particles per m^3 of air and δm_i is the mass of each particle with diameter d_i .

The scattering cross-section, σ_i , for each particle size diameter, d_i , at the selected wavelength can be calculated using either Rayleigh or Mie scattering theory, depending on the particle size relative to the wavelength. Then, the scattering coefficient and the mean free path of a photon propagating through moist air containing the above size distribution of water particles are determined by

$$\mu_s = \sum_i \rho_i \sigma_{s,i}, \quad \bar{l}_f = \frac{1}{\mu_s}. \quad (22)$$

The probability of a photon scattered by a particle with diameter d_i is given by

$$p_i = \frac{\rho_i \sigma_i}{\mu_s} = \rho_i \sigma_i \bar{l}_f. \quad (23)$$

As far as the scattering angle is concerned, there is no dependence on the particle diameter for Rayleigh scattering. For Mie scattering, the probability distribution of the scattering angle can be generated using (19) for any value of d .

D. PHOTON ABSORPTION

A photon may be absorbed from an atmospheric particle or a surface triangle. The probability of atmospheric absorption in dry air or air containing spherical water particles is two to three orders of magnitude lower than the scattering probability. The probability of atmospheric absorption becomes significant only if the atmosphere contains particles different than water. Thus, in our scenarios, atmospheric absorption is considered negligible.

The probability of photon absorption by a surface triangle is defined as one minus the albedo (reflectivity) of the triangle. It is the primary means of UV energy deposition on the triangle, which could be used for communication disinfection purposes.

III. COMPUTATIONAL MODELING OF LIGHT PROPAGATION IN THE AIR

A. ADJUSTABLE PHYSICAL QUANTITIES AND PRECALCULATION OF LOOKUP TABLES

LaUV allows setting the values of the main physical properties to simulate various atmospheric conditions and assess the applicability of the UV light effect in applications including disinfection and communications. Specifically, the implemented mathematical model allows the user to set the wavelength of the emitted radiation, the temperature, and the atmosphere composition, namely, the relative humidity and particle densities for several diameters. The simulator can be applied to indoor (or even outdoor) settings, including any number of triangulated objects of arbitrary shape. In addition, the albedo and the roughness of each triangle can be defined.

To accelerate the algorithm execution, we have precalculated and stored in text files the Mie scattering cross sections for all combinations of wavelengths and particle diameters in Table 1, using (11)-(13), respectively. For the same combinations of λ and d , the probabilities for all Mie scattering angles have also been precalculated using (19) and stored. The probabilities for pre-specified angles are also calculated for Rayleigh scattering, independently of the particle diameter. Finally, the scattering cross-section and the probabilities for intermediate wavelength or particle diameter values can be calculated using linear interpolation.

TABLE 1. The values of λ and d used for lookup tables precalculation.

Symbol	initial value : step : final value
λ (nm)	200 : 10 : 300
d (nm)	1 : 1 : 100, 100 : 100 : 5000
θ ($^\circ$)	0 : 1 : 180

B. ALGORITHM FOR SINGLE-PHOTON PROPAGATION

Algorithm 1 summarizes the UV photon propagation as implemented in the present study. The inner WHILE loop tracking each photon terminates when the air or the surface has absorbed it, or the photon has "gone away", i.e., being

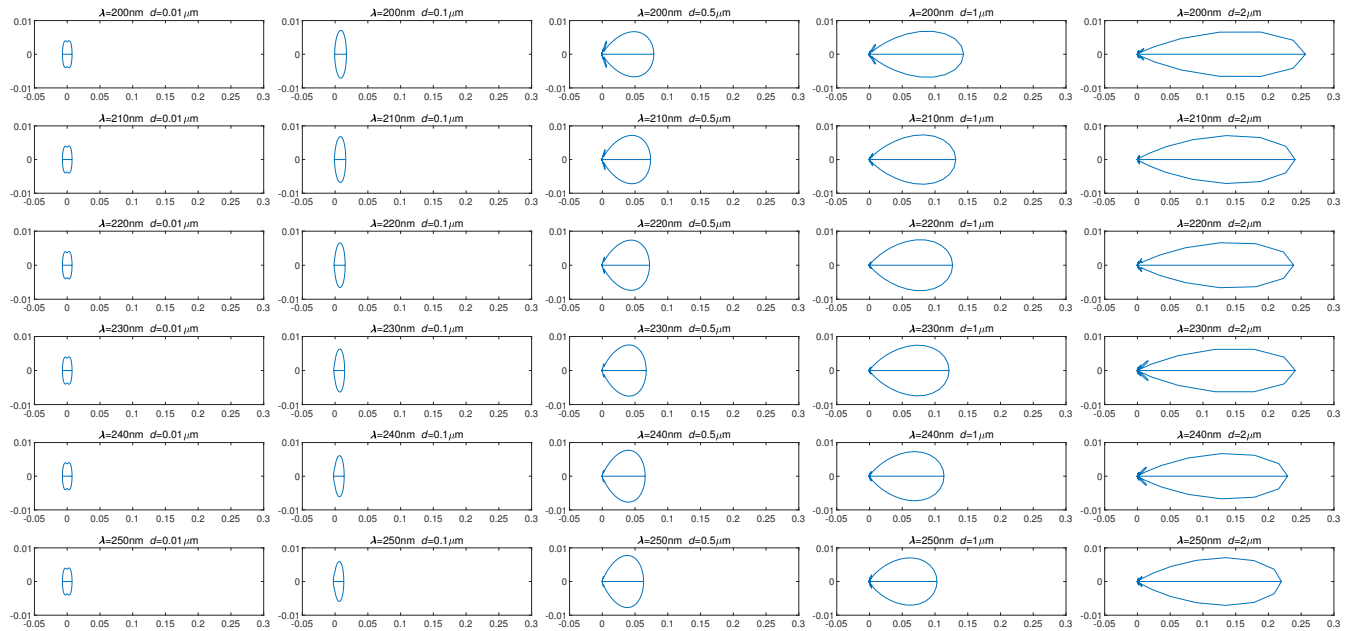


FIGURE 3. Probability distribution for Mie scattering at a specific angle relative to the incident radiation for different values of λ and d .

at a distance greater than a predetermined threshold from the modeled scene. The later condition ("gone away") enables the application of the algorithm to outdoor or not fully closed indoor scenes; if a photon can move away from the scene of interest in these scenes, where the MC algorithm has to stop tracing the photon. Moreover, the algorithmic steps are shown graphically in Fig. 4. The mathematical formalism of the atmospheric scattering and surface reflection are described in detail in the following section.

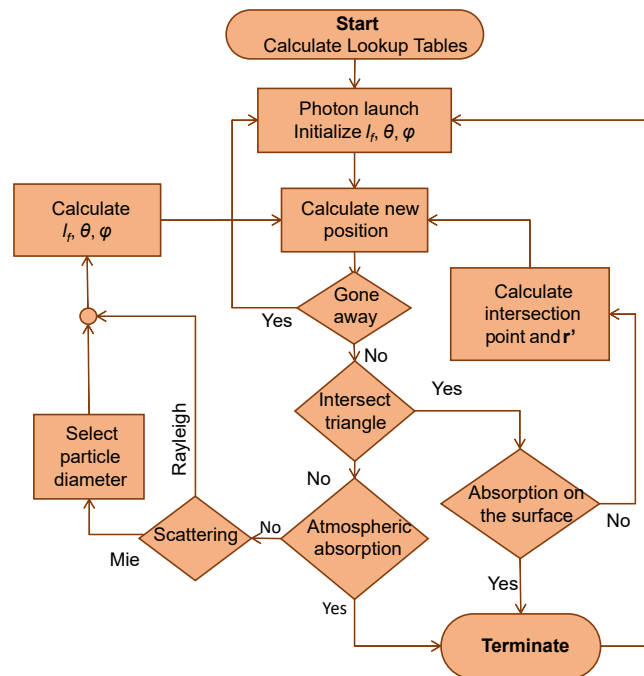


FIGURE 4. Schematic diagram of the proposed photon propagation algorithm.

C. RANDOM SCATTERING ANGLE GENERATION

In general, it is not always possible to calculate the inverse function of the cumulative probability distribution of $p(\theta)$. Therefore, we employ the following steps to generate the random scattering angles. First, $p(\theta_i)$ is discretized for $\theta_i = i\delta\theta$, $i = 0, 1, 2, \dots$ and $\delta\theta = 1^\circ$. The cumulative probability, $c_i = \sum_{k=0}^i p(\theta_k)$, is then calculated for all discrete angles, θ_i .

Each time a random angle is required, a random number, r , is generated using the uniform distribution in $[0, 1]$, and the consecutive elements of the cumulative probability c_i , $c_i - 1$ are determined so that $c_{i-1} \leq r < c_i$. To obtain continuous random angles, θ_i , linear interpolation applies to the corresponding angles, θ_i, θ_{i-1} , using the following equation

$$\theta = \theta_{i-1} \frac{c_i - r}{c_i - c_{i-1}} + \theta_i \frac{r - c_{i-1}}{c_i - c_{i-1}}. \quad (24)$$

The above method applies to generate random scattering angles for both Rayleigh and Mie scattering using (2) and (19), respectively as $p(\theta_i)$.

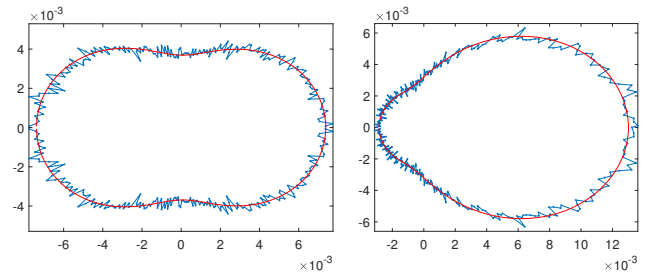
To verify the method, 100,000 random angles were calculated for Rayleigh and Mie scattering. In Mie scattering, the wavelength was set to 254 nm , and a particle diameter of 100 nm was selected.² The histograms of the generated random angles are calculated with a bin size of 1 degree. The two histograms are plotted in polar coordinates in Fig. 5. The theoretical probability distributions according to (2) and (19) are also overlaid.

²This wavelength was selected as an example since a peak of disinfection efficiency has been observed at $\lambda = 254 \text{ nm}$ and 222 nm , according to [11], [14].

Algorithm 1: Photon propagation algorithm

Input: Faces and vertices of the triangulated surface, A for each triangle, $R_H, T, \lambda, d_0, \alpha, \gamma, d_i$, sources' location
Output: For each triangle: exposure, prevalent phenomenon, total path lengths of each absorbed photon
Init: d_i and ρ_i, μ_{sR} and $\mu_{sM}, p(\theta)$, triangle normal vectors \mathbf{n}

for each photon do
 | Initialize starting coordinates, θ, φ , and l_f
while photon has not been absorbed or gone away do
 | Calculate new photon position using (27)
 | **if no trajectory intersection with any triangles then**
 | | **if Atmospheric absorption then**
 | | | **break** Launch new photon
 | | **else**
 | | | Calculate scattering probabilities
 | | | $p_R = \frac{\mu_{sR}}{\mu_{sM} + \mu_{sR}}$ (Rayleigh) and
 | | | $p_M = \frac{\mu_{sM}}{\mu_{sM} + \mu_{sR}}$ (Mie)
 | | | Select $\xi \sim \cup(0, 1)$
 | | | **if Rayleigh scattering then**
 | | | | $l_f \leftarrow l_{fR} = -\frac{\ln \xi}{\mu_{sR}}$
 | | | | Select θ from (2)
 | | | **else**
 | | | | $l_f \leftarrow l_{fM} = -\frac{\ln \xi}{\mu_{sM}}$
 | | | | Select d_i from (23), θ from (19), and φ ,
 | | | | uniformly distributed in $[0, 2\pi]$
 | | **else**
 | | | Determine the nearest triangle, Δ_i , as the intersecting one
 | | | Select $\xi \sim \cup(0, 1)$
 | | | **if $\xi < A(\Delta_i)$ then**
 | | | | $exposure(\Delta_i) = exposure(\Delta_i) + 1$
 | | | | **break** Launch new photon
 | | | **else**
 | | | | Current photon coordinates \leftarrow reflection point
 | | | | Calculate \mathbf{r}' , and the remaining l_f
 | | | | Calculate new photon coordinates using (27)



Rayleigh scattering (irrespective of λ and d) Mie scattering for $\lambda = 254 \text{ nm}$ and $d = 100 \text{ nm}$

FIGURE 5. The theoretical scattering angle distribution (smooth red curve) and the histogram of the generated random angles (blue curve).

It can be confirmed that $\theta_i = \cos^{-1}(\hat{\mathbf{p}} \cdot \mathbf{s})$ with $\hat{\mathbf{p}} = \mathbf{p}/|\mathbf{p}|$. When the z component of the unit \mathbf{p} vector is greater than 0.99999, the above formula is modified as [44, eq. (12)]

$$\begin{aligned} x' &= \sin \theta_i \cos \varphi_i, \\ y' &= \sin \theta_i \sin \varphi_i, \\ z' &= -\frac{z}{|z|} \cos \varphi_i. \end{aligned} \quad (26)$$

The geometry of the scattering process is illustrated in Fig. 6. It is easy to confirm that \mathbf{s} is a unit vector. The new photon position, Q_{i+1} , relative to its current location, Q_i , is determined as

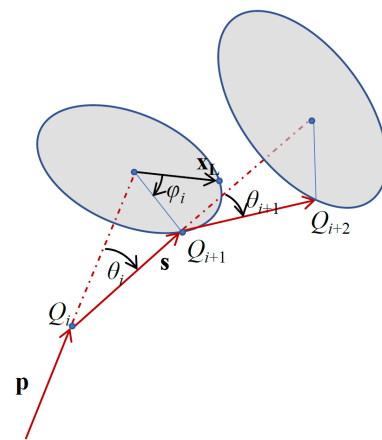


FIGURE 6. The geometry of atmospheric scattering.

$$Q_{i+1} = Q_i + s l_f, \quad (27)$$

where l_f is calculated as described in Algorithm 1.

D. PHOTON ATMOSPHERIC SCATTERING

Photons are scattered by atmospheric molecules or particles during propagation, causing a change in the propagation direction. The following mathematical description applies both to Rayleigh and Mie scattering.

Let Q_i be the photon's current position and $\mathbf{p} = (x, y, z)$ the incident vector to this position. If an atmospheric particle scatters the photon with scattering angle, θ_i , and azimuthal angle, φ_i , the scattering vector $\mathbf{s} = (x', y', z')$ is calculated through the formulae [44, eq. (11)]

$$\begin{aligned} x' &= \frac{\sin \theta_i}{\sqrt{1 - z^2}} (xz \cos \varphi_i - y \sin \varphi_i) + x \cos \theta_i, \\ y' &= \frac{\sin \theta_i}{\sqrt{1 - z^2}} (yz \cos \varphi_i - x \sin \varphi_i) + y \cos \theta_i, \\ z' &= -\sin \theta_i \cos \varphi_i \sqrt{1 - z^2} + z \cos \varphi_i. \end{aligned} \quad (25)$$

E. PHOTON REFLECTION FROM SURFACES

When a photon propagating from its current position, Q_i , along the incident vector, $\mathbf{p} = Q_{i+1} - Q_i$, intersects a surface triangle with a normal vector, \mathbf{n} , at the point C , it will either be absorbed or reflected, according to the triangle albedo. If the incident surface is smooth, the reflection is perfect, and

the reflected unit vector, \mathbf{r} , is calculated through the formula [45]

$$\mathbf{r} = \hat{\mathbf{p}} - 2(\hat{\mathbf{p}} \cdot \mathbf{n}) \cdot \mathbf{n}, \quad (28)$$

where $\hat{\mathbf{p}} = \mathbf{p}/|\mathbf{p}|$. The above three vectors lie on the same plane and are defined so that $\cos(\hat{\mathbf{p}} \cdot \mathbf{n}) < 0$ and $\cos(\mathbf{r} \cdot \mathbf{n}) > 0$. The angles of incidence and perfect reflection are equal.

If the reflecting surface is rough, the reflected vector \mathbf{r}' deviates from the perfect reflection vector \mathbf{r} by an angle ω ; thus, \mathbf{r}' is not necessarily at the same plane as \mathbf{p} , \mathbf{r} , and \mathbf{n} . The angle ω is randomly set using the normal distribution with zero mean and standard deviation $\Sigma = 1$ rad. The value of Σ defines the roughness of the surface and can be set for each triangle individually. Values of Σ close to 0 indicate ideal, or very specular reflection, whereas greater values bring about diffuse reflection. Care has been taken so that the angle between \mathbf{n} and \mathbf{r}' is less than 90° . The new photon position after the surface reflection is given by

$$Q'_{i+1} = C + \mathbf{r}'(l_f - |C - Q_i|). \quad (29)$$

The reflection as described above is depicted in Fig. 7.

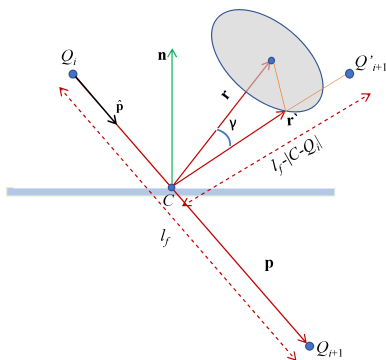


FIGURE 7. Schematic representation of the reflection process for specular reflection.

F. IDENTIFYING TRIANGLE-LINE SEGMENT INTERSECTIONS IN 3D

For each linear segment of a photon path, its intersection is checked with all triangles comprising the modeling scene. If such intersecting triangles exist, the intersection point closest to Q_i is determined. For this purpose, the algorithm by Möller and Trumbore was employed in [46] as implemented in [47].

IV. NUMERICAL RESULTS

A. SIMULATION SCENARIOS

A scene consisting of a closed room of dimensions $5 \times 5 \times 5$ m, with and without furniture is considered. One or two light sources are used, placed at positions (1.5, 2.5, 3) and (3.5, 2.5, 3), each emitting 1,000,000 photons isotropically downwards. The origin of the reference system is set one at

the floor corners of the room, whereas all length units are in meters.

Several different scenarios have been simulated. In every scenario, the wavelength is considered 250 nm, and three different cases of particle diameter distribution are chosen, based on the modified gamma distribution (20) with the most frequent particle diameter, d_0 , equal to 2 nm, 20 nm, and $4 \mu\text{m}$, respectively. The first value corresponds to the atmospheric conditions with the highest visibility. The second corresponds to conditions with condensed humidity and low visibility, whereas the droplets with $d_0=4 \mu\text{m}$ (3rd value) are generated mainly by nebulizers. These combinations are summarized in Table 2.

TABLE 2. Summary of the different scenarios investigated.

$d_0 = 2 \text{ nm}$	$d_0 = 20 \text{ nm}$	$d_0 = 4 \mu\text{m}$
$A = 0.1$		
Scenario 1a $\mu_s = 0.02 \text{ m}^{-1}$	Scenario 2a $\mu_s = 5.07 \text{ m}^{-1}$	Scenario 3a $\mu_s = 6.7 \text{ m}^{-1}$
$A = 0.5$		
Scenario 1b $\mu_s = 0.02 \text{ m}^{-1}$	Scenario 2b $\mu_s = 5.07 \text{ m}^{-1}$	Scenario 3b $\mu_s = 6.7 \text{ m}^{-1}$

The surface albedo values were set to 0.1 and 0.5, respectively. The first value approximates the UV-C albedo for most materials, while only specific materials exhibit UV-C albedo values as high as 0.5 [48], [49]. The rest of the simulator parameters were kept constant for all scenarios with the following typical values, $R_H = 50\%$ and $T = 20^\circ\text{C}$, $\alpha = 3$, and $\gamma = 0.543$. Details of the aforementioned parameters for scenarios 1, 2, and 3 are highlighted in Tables 3, 4, and 5, respectively.

TABLE 3. Scenario 1 ($R_H = 50\%$, $T = 20^\circ\text{C}$, $\lambda = 250 \text{ nm}$, $d_0 = 0.002 \mu\text{m}$, $\alpha = 3$, $\gamma = 0.543$).

$\rho \text{ (m}^{-3}\text{)}$	$d \text{ (}\mu\text{m)}$	π	$\mu_{si} \text{ (m}^{-1}\text{)}$	$\sigma_s \text{ (m}^2\text{)}$
Rayleigh scattering, $\mu_s = 0.0237 \text{ m}^{-1}$				
4.26×10^{19}	0.5	0.141	2×10^{-9}	4.0×10^{-29}
8.19×10^{19}	0.8	0.272	6×10^{-8}	6.7×10^{-28}
1.04×10^{20}	1	0.344	3×10^{-7}	2.6×10^{-27}
6.51×10^{19}	5	0.216	0.003	4.0×10^{-23}
8.19×10^{18}	10	0.027	0.021	2.6×10^{-21}
Mie scattering, $\mu_s = 0.0004 \text{ m}^{-1}$				
9.59×10^{12}	50	3×10^{-8}	0.001	3.9×10^{-17}
0	500	0	0	7.8×10^{-13}
0	1000	0	0	1.7×10^{-12}
0	2000	0	0	7.7×10^{-12}

Figure 8 demonstrates the simulation results of the propagation of a parallel photon beam (red line), consisting of 100 photons under each of the above six scenarios. The trajectory

TABLE 4. Scenario 2 ($R_H = 50\%$, $T = 20^\circ C$, $\lambda = 250$ nm, $d_0 = 0.02$ μm , $\alpha = 3$, $\gamma = 0.543$).

ρ (m^{-3})	d (μm)	π	μ_{si} (m^{-1})	σ_s (m^2)
Rayleigh scattering, $\mu_s = 0.0005$ m^{-1}				
5.45×10^{14}	0.5	0.001	2×10^{-14}	4.0×10^{-29}
1.80×10^{15}	0.8	0.004	1×10^{-12}	6.7×10^{-28}
3.10×10^{15}	1	0.007	8×10^{-12}	2.6×10^{-27}
8.51×10^{16}	5	0.199	3×10^{-6}	4.0×10^{-23}
2.07×10^{17}	10	0.484	0.001	2.6×10^{-21}
Mie scattering, $\mu_s = 5.0669$ m^{-1}				
1.30×10^{17}	50	0.304	5.502	3.9×10^{-17}
1.92×10^{17}	500	4×10^{-8}	0.015	7.8×10^{-13}
77433	1000	2×10^{-13}	1×10^{-7}	1.7×10^{-12}

TABLE 5. Scenario 3 ($R_H = 50\%$, $T = 20^\circ C$, $\lambda = 250$ nm, $d_0 = 4$ μm , $\alpha = 3$, $\gamma = 0.543$).

ρ (m^{-3})	d (μm)	π	μ_{si} (m^{-1})	σ_s (m^2)
Rayleigh scattering, $\mu_s = 0.0237$ m^{-1}				
45635	0.5	1×10^{-7}	2×10^{-24}	4.0×10^{-29}
115880	0.8	4×10^{-7}	8×10^{-23}	6.7×10^{-28}
180222	1	5×10^{-7}	5×10^{-22}	2.6×10^{-27}
4256231	5	1×10^{-5}	2×10^{-16}	4.0×10^{-23}
1628157	10	5×10^{-5}	4×10^{-14}	2.6×10^{-21}
Mie scattering, $\mu_s = 6.705$ m^{-1}				
3.34×10^8	50	0.001	1×10^{-8}	3.9×10^{-17}
1.43×10^{10}	500	0.043	0.011	7.8×10^{-13}
3.31×10^{10}	1000	0.101	0.056	1.7×10^{-12}
5.99×10^{10}	2000	0.182	0.461	7.7×10^{-12}
7.24×10^{10}	3000	0.220	1.025	1.4×10^{-12}
7.55×10^{10}	4000	0.230	2.276	3.0×10^{-11}
7.34×10^{10}	5000	0.223	2.876	3.9×10^{-11}

ries of the photons until they are absorbed are visualized in blue. The red dot represents the single source, positioned at (3.5, 2.5, 3).

Scenarios 1b, 2b, and 3b reveal a greater diffusion of the photon distribution compared to scenarios 1a, 2a, and 3a, respectively. That is due to the high albedo value, i.e., the surface reflection. In scenarios 1a and 1b, the most frequent particle diameter equals $d_0 = 2$ nm, and hence Rayleigh scattering prevails. Due to the small μ_s , the mean free path length of the photons, l_f , is approximately 20 m, so the propagation in a room of these dimensions is almost along straight lines, between surface reflections. In contrast, in scenarios 2a and 2b, where μ_s is high, intense scattering occurs, as can be confirmed from Fig. 3. The most probable particle diameter, d_0 , equals 20 nm; therefore, the Mie scattering prevails with a more uniform angle distribution. In scenarios 3a and 3b, Mie scattering also prevails, however mainly forward scattering appears due to the high value of $d_0 = 4 \mu m$ (see Fig. 3) with the most probable scattering

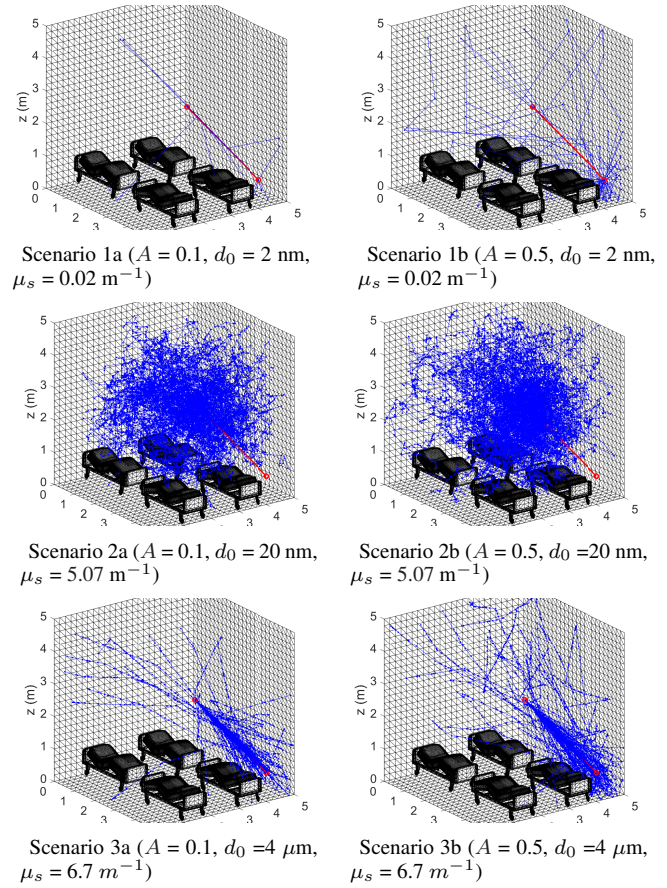


FIGURE 8. A parallel photon beam of 100 photons, shown in red and their trajectories until absorbance.

angle equal to few degrees. Therefore, despite the significant value of μ_s , the beam does not exhibit substantial divergence within the room dimensions.

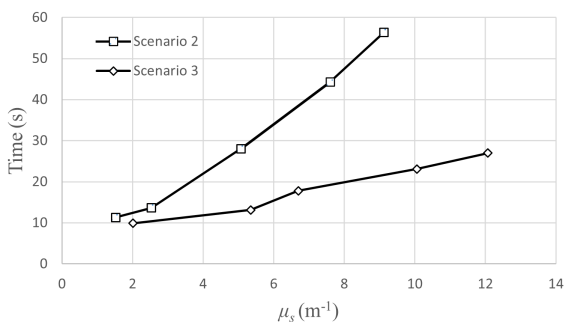
LaUV has been implemented using the Matlab (Mathworks) programming environment. Typical execution times on a typical laptop (Intel (R) Core (TM) i5 1035G1 CPU 1 GHz 1.19 GHz, 8GB RAM) for scenario 1a (1 million photons) and 185,548 triangles were approximately 2.5 hours.

The computational complexity of LaUV can be theoretically computed, especially in closed rooms, where the proposed algorithm simulates each photon until it is absorbed. In open scenes, the simulator stops tracking photons when their distance from the scene becomes greater than a pre-defined threshold (“gone-away” algorithmic check).

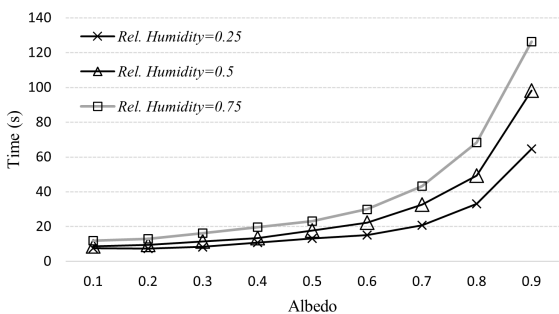
The scattering coefficient, μ_s , is expected to have strong effect on execution time: as the value of μ_s increases, the mean free path l_f becomes smaller and atmospheric scattering becomes more frequent for each photon. Consequently, the algorithmic steps involving selecting scattering-type, angle, and calculation of the new position (including checking for surface reflections) are executed more frequently. It is, therefore, safe to conclude that increasing μ_s will cause execution time to increase.

However, changes in μ_s value can be a result of change of

temperature and relative humidity, or change of the diameter distribution of water nanoparticles, which affects the Mie scattering angle distribution (phase function). More specifically, an almost uniform scattering angle distribution (due to small particle diameter), combined with a high μ_s value, will result in many photon scatterings before a photon - surface collision occurs. On the other hand, a scattering angle distribution that favors forward scattering will result in photon - surface collisions after fewer atmospheric scatterings. This can be observed in Fig. 8 (scenarios 2a and 2b vs. 3a and 3b), where although the μ_s does not alter significantly (5.07m^{-1} vs 6.7m^{-1}), the effect of the different phase functions due to different particle diameter distribution is profound. Therefore, it is expected that a change in μ_s will have a strong effect on the execution time in the case of a more uniform distribution of scattering angle (such as in scenario 2). On the other hand, in the case of larger diameter nanoparticles that favor forward scattering (such as in scenario 3), the effect of μ_s on the execution time should be less profound. This can be observed experimentally in Fig. 9, where the execution time of LaUV is shown against different values of μ_s for scenarios 2 and 3, caused by changing the R_H only (the phase function remained unaffected for each scenario), keeping $A = 0.5$. A number of 10,000 photons have been considered, using the same computer hardware. It is evident that in the case of scenario 3, the increase of execution time, as a result of increasing μ_s , is linear with a smaller gradient, compared to the corresponding increase in the case of scenario 2.



The effect of μ_s on execution time for scenarios 2 and 3, for $A=0.5$.



The effect of A on execution time for scenario 3.

FIGURE 9. The computational complexity (execution times) of the proposed LaUV. Times are provided for the empty room with 7500 triangles and 10,000 photons.

In the closed room case, the surface albedo is also expected to affect the execution time, i.e., low values of the albedo cause a low probability of a photon surviving a surface reflection. Therefore, it would lead to short execution times, whereas albedo values close to 1 (non-realistic for most materials for UV-C light) would cause very long execution times. More formally, for constant A , a photon probability not being attenuated after n surface reflections is A^n . Thus, the necessary number of surface reflections to reach a probability of non-attenuation equal to or less than 0.01 is $n \geq \frac{-2}{\log_{10} A}$, which shows that the necessary number of surface reflections for a photon to be absorbed, increases exponentially as A approaches the value of 1. This behavior can be observed clearly in Fig. 9, where the execution times for 10,000 photons are provided for scenario 3, for three different values of R_H . The number of triangles is also expected to affect the execution time, precisely the algorithmic step that checks for triangle–line segment intersection in 3D.

Since scenarios 3a and 3b resemble scenarios 1a and 1b in terms of photon trajectories, despite the different atmospheric conditions, we give a particular focus on scenarios 1a, 1b, 2a, and 2b in the rest of the current section. The light sources considered for each selected scenario are indicated by red dots. The following quantities are graphically depicted using a standard scale for comparison:

- exposure, indicated by the number of absorbed photons per cm^2 for each elementary triangle, which is proportional to UV exposure rate
- the prevalent phenomenon in the deliverance of exposure in each triangle, as described in the next paragraph
- the mean total path length of the photons, \bar{L} , ended up in each triangle

B. EMPTY ROOM

Scenarios 1a and b and 2a and b were simulated in the room without any furniture. The primary purpose is to investigate the behavior of UV light in a simpler environment before introducing more complicated geometric objects.

1) Prevalent phenomenon per triangle

Figure 10 shows the prevalent phenomenon in each triangle (direct line-of-sight (LOS), reflection, and scattering). The following color-encoding applies, including cases of more than one phenomenon being equally strong:

- blue triangles: LOS - the majority of the absorbed photons in these triangles arrived without sustaining scattering or reflection
- green triangles: Reflection - the majority of the absorbed photons in these triangles arrived after at least one reflection, without sustaining scattering
- red triangles: Scattering - the majority of the absorbed photons in these triangles arrived after at least one scattering, without sustaining reflection
- light blue triangles: LOS and reflection equally prevail
- yellow triangles: Reflection and scattering equally prevail

- purple triangles: LOS and scattering equally prevail
- white triangles: LOS, reflection, and scattering equally prevail
- black triangles: no photons have been collected

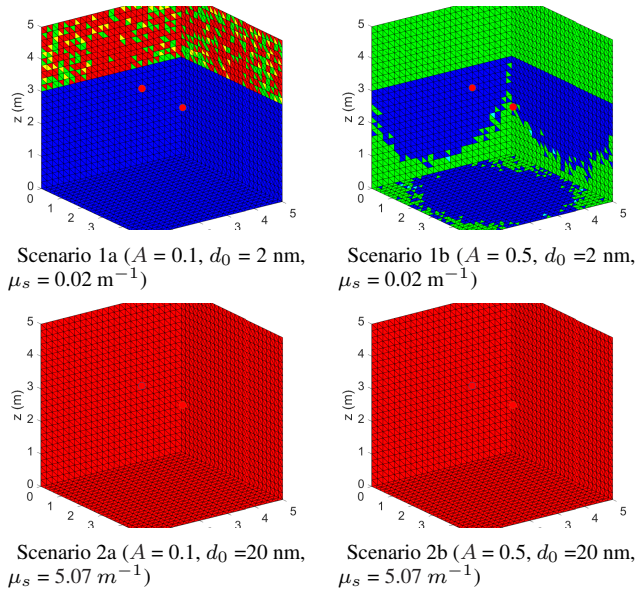


FIGURE 10. The prevalent phenomenon per triangle.

It is noticed that for small μ_s and low albedo, LOS prevails in almost all triangles with direct LOS with the sources (blue color). In the NLOS triangles (barycenter z -coordinate > 3 m), photons can end up only by reflection (green color) or scattering (red color). In scenario 1b ($A = 0.5$), reflection prevails in triangles close to the wall edges and triangles with z -barycenter coordinate larger than the sources (3 m). Due to the specific room dimensions and sources' arrangement, floor triangles close to edges receive more photons than wall triangles close to edges. (Although at the same distance from the source, the incoming LOS photons are more perpendicular to the floor triangles than wall triangles, closer to edges). That can also be confirmed in Fig. 12. In case of significant surface reflection (high A), more reflected photons end up in wall triangles close to the edges than the reflected photons absorbed in floor triangles (close to edges). This phenomenon diminishes when the albedo obtains low values. These can be verified in Fig. 11, scenario 1a and 1b. Meanwhile, for large values of μ_s (scenario 2a, 2b), scattering prevails in most triangles, as expected (red color in Fig.10, right column).

2) UV exposure

Figure 11 quantifies the UV exposure (equivalently the number of absorbed photons per cm^2) for each elementary triangle using a standard color scale. In scenarios 1a and 1b, Rayleigh scattering occurs due to the small d_0 value. The atmospheric scattering is less frequent (μ_s has small values, and $l_f = 1/\mu_s = 50$ m), so LOS prevails (triangle with blue color in Fig. 10). More photons end up in triangles with a small distance from the photon sources and a higher impact

angle in all scenarios. Differences in absorbed photons in scenarios 1a and 1b are attributed to the different surface albedo. In scenario 1b, greater diffusion of the absorbed photon occurs, mainly in triangles with NLOS (triangles with barycenter z -coord. > 3 m), compared to scenario 1a due to the higher albedo. In scenarios 2a and 2b, the increased μ_s value compared to scenarios 1a and 1b causes absorbed photons to be diffused in larger areas of the walls. That becomes particularly obvious on the floor and in NLOS areas. The increased absorption shown on the wall at $x = 0$ is due to the small distance of one of the sources (minimum distance of only 1.5m from the source 1) and the overlaid projection of the 2nd source. The differences between scenarios 2a and 2b are less visible in the current color scale.

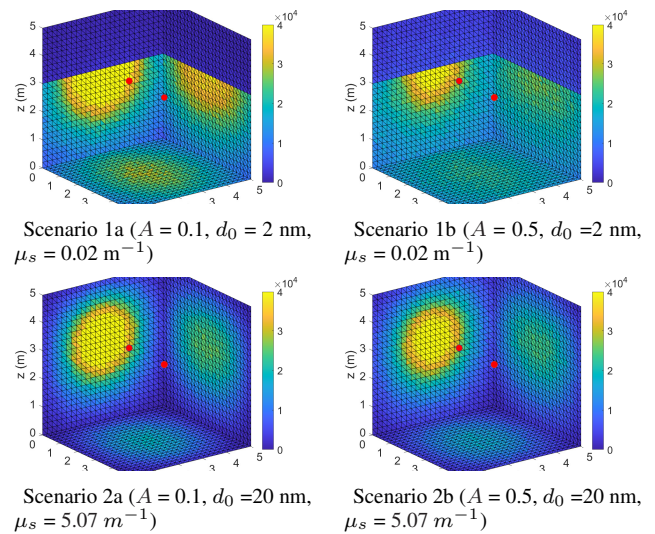


FIGURE 11. The exposure (absorbed photons per cm^2) in each triangle.

For all scenarios, fewer photons are absorbed in the corners of the room, with this phenomenon being more profound in scenarios 2a and 2b due to increased scattering. Lower values of the albedo further enhance this phenomenon. In scenarios 2a and 2b, μ_s has a considerable value; thus, the mean free path is very short, resulting in many scatterings per photon. Therefore, scattering is the prevailing phenomenon in almost all triangles. In addition, the small diameter of the water particles results in an almost uniform distribution of the scattering angle. Consequently, the exposure difference between LOS and NLOS areas becomes diminished. Although scenarios 2a and 2b appear to have very similar absorbed photon distributions, the increased reflection caused by higher albedo in scenario 2b smooths the considerable differences between centers of the walls and corner areas. That will become more apparent in the following subsection, where a furnished room is studied.

3) Mean total path length

Figure 12 depicts the mean length of the total path, \bar{L} , of the photons absorbed in each triangle for an empty room, using a standard color scale for comparison. In scenario 1a,

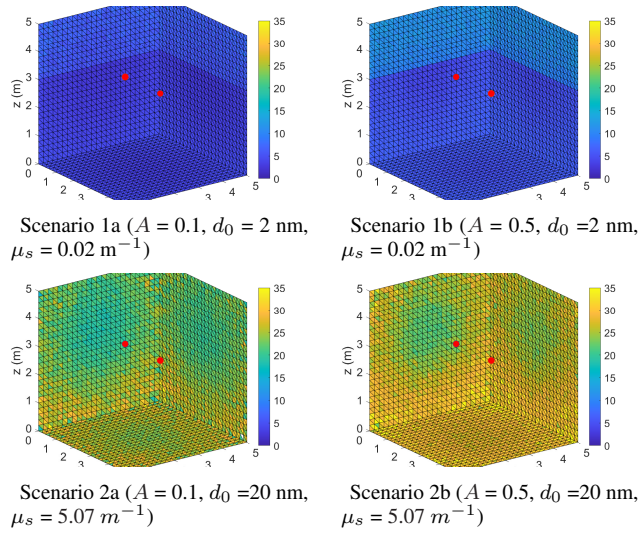


FIGURE 12. The mean total path length of the photons absorbed in each triangle.

the \bar{L} value for each triangle is smaller than scenario 1b due to the increased surface albedo of the latter, which induces a significant number of surface reflections. In scenarios 2a and 2b, \bar{L} significantly increases compared to scenarios 1a and 1b due to the larger value of μ_s . Additionally, the difference in albedo between scenarios 2a and 2b causes the mean total free length to increase in 2b. It is of interest that in an empty room of dimensions $5 \times 5 \times 5m$, \bar{L} ranges between 5 m (low μ_s , low A) to over 35 m (high μ_s , high A). Triangles close to the sources exhibit an \bar{L} value less than that of more distant triangles, as expected. That becomes more apparent in scenarios 2a and 2b.

4) CIR

By assuming that all photons are simultaneously emitted from the sources at time $t = 0$, the temporal distribution of the photons absorbed per cm^2 in any triangle over their total path length becomes equivalent to CIR, since the total path length can be converted into the time of arrival (ToA). Figure 13 indicates the two characteristic points for the empty room: point A on the floor directly under one of the sources (source position: (1.5, 2.5, 3) m) and point B close to the corner. The CIR for points A and B, for scenarios 1a and 2a, are illustrated in Fig. 14. In both scenarios, the CIR for A is much sharper than for B, which appears flattered and delayed. There is a marked difference between the CIRs for the same points between the two scenarios: in scenario 2a, the CIRs for both points exhibit a long tail towards the right, with delayed appearance of the peak, compared to scenario 1a.

C. ROOM WITH FURNITURE

In what follows, the same scenarios were executed in the more realistic case of inserting four beds in the room, resembling a hospital room. The beds consist of approximately

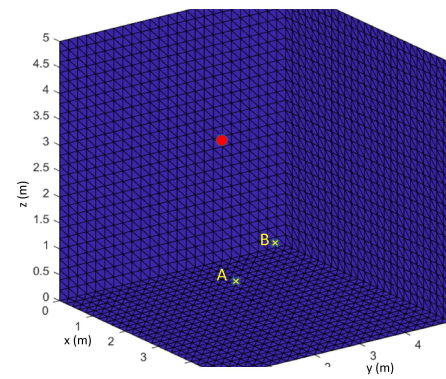


FIGURE 13. The two selected points (A and B) in the empty room.

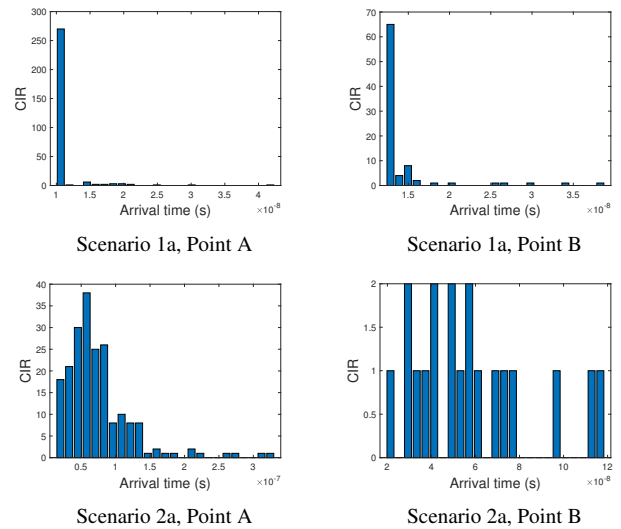


FIGURE 14. The CIR at the two selected points, for scenarios 1a ($A = 0.1$, $d_0 = 2$ nm, $\mu_s = 0.02$ m^{-1}) and 2a ($A = 0.1$, $d_0 = 20$ μm , $\mu_s = 5.07$ m^{-1}), measured for the nearest light source only

44512 triangles arranged realistically, referring to an ordinary hospital room.

1) Prevalent phenomenon

Figure 15 demonstrates the phenomenon that prevails in each triangle (blue for LOS, green for reflection, and red for scattering). The prevalent phenomena in every scenario defined above are similar to those of the empty room. The main difference is that the reflection becomes the prevalent phenomenon under the beds (green color) and close to the edges, especially in scenario 1b (low μ_s , high A , as observed in Fig. 16 that zooms into one of the beds). The latter can be explained as follows: in scenario 1b (empty room), the triangles of the walls close to the edges receive many photons reflected from the floor. The inclusion of beds caused the reflected photons to end up at higher triangles, where the LOS continues to be the prevalent phenomenon due to the better orientation and smaller distance from the sources.

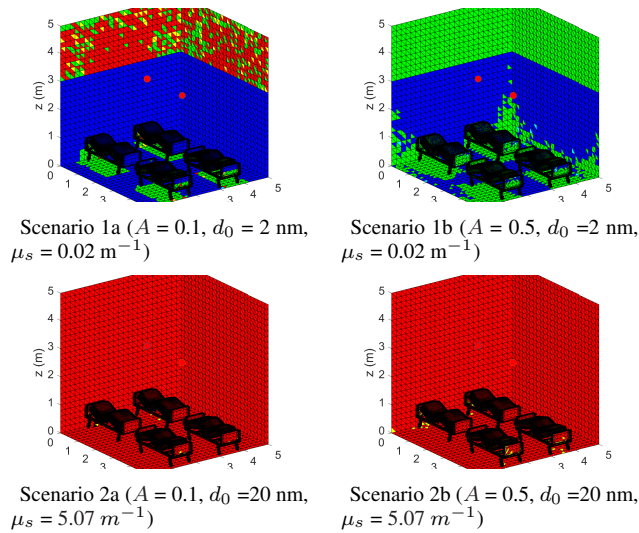


FIGURE 15. The prevalent phenomenon per triangle.

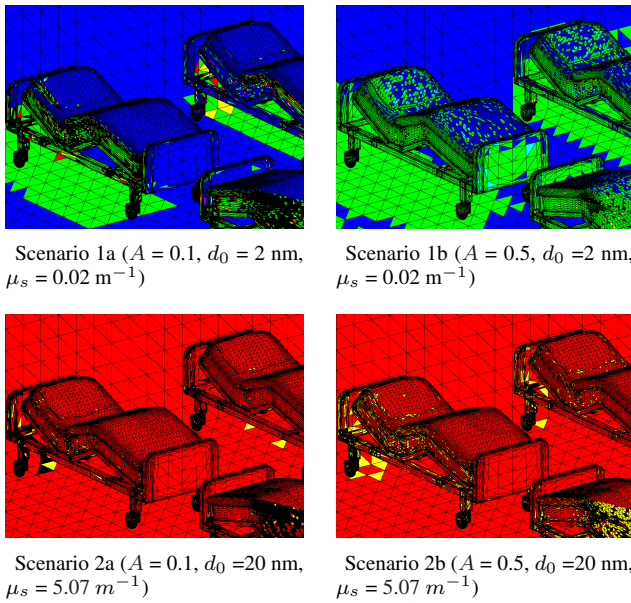


FIGURE 16. Details of the prevalent phenomenon in areas close to the beds.

2) UV exposure

Figure 17 illustrates the UV exposure for each elementary triangle of the scene, using a common color scale for comparison. The distribution of exposure in the furnished room is similar to the empty one in Scenario 1a. However, the distribution of exposure in Scenario 1b changes significantly with the inclusion of beds. The high A value and the large numbers of triangles with random orientation, introduced by the beds, distribute the absorbed photons more equally among the room triangles. That is evident in NLOS areas, such as the wall triangles with $z > 3$ m and the triangles under the beds, where the number of absorbed photons increases in scenario 1b as shown in Fig. 18. In scenarios 2a and 2b, the atmospheric composition of water droplets

favors Mie scattering, and μ_s obtains high values, resulting in many photons' absorption in triangles near the ceiling and not near the corners, as discussed in Fig. 17. Furthermore, the increased reflection caused by higher albedo in scenario 2b smooths the significant differences between the centers of the walls and corner areas significantly, as shown in Fig. 17 at a lesser degree.

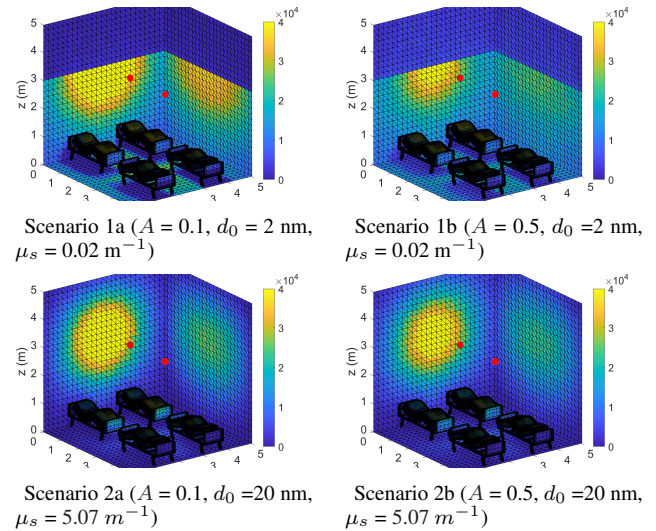


FIGURE 17. The UV exposure in each triangle.

Figure 18 highlights the exposure on several bed surfaces as well as beneath the bed, which is essential when using UV-C light for sterilization purposes. As observed in scenario 1a, parts of the beds with direct LOS receive between 25.000 and 35.000 photons/cm² for 2×10^6 emitted photons, whereas areas without LOS, such as under the bed, receive on average 1000 photons/cm². This situation slightly improves in 2a and gets significantly enhanced in scenario 1b.

To study the results in a more comprehensive manner, four characteristic points are selected, depicted as A, B, C, and D in Fig. 19 (on the pillow facing up, at the side of the pillow, at the side of the bed and under the bed respectively). Point A is in LOS, and point B is marginally in LOS. Points C and D are definitely in NLOS; however, photons reach point C more easily than D. The exposure at each of the 4 points is provided in Table 6 for the four different scenarios, considering 2×10^6 emitted photons. The relative exposure at point A (LOS) is also shown. Point A receives the highest exposure in all scenarios due to LOS, as expected. The rest of the points receive photons by scattering or reflection, so their exposure is significantly lower. It can be observed that in scenarios 1a and 2a, the low albedo causes the NLOS points B, C, and D to receive a tiny fraction of photons with respect to the LOS point A, irrespective of the μ_s value. In scenarios 1b and 2b, the high A value makes the fraction of exposure in the NLOS points (C, D) increase significantly. Among them, scenario 1b (high A , low μ_s) appears to maximize this fraction considering point D, an NLOS point hard to reach by the photons. That is an important finding since it directly impacts light

TABLE 6. Number and fraction of photons absorbed in four characteristic points of the beds assuming 2×10^6 photons emitted from the two sources.

Points	Scenario 1a		Scenario 1b		Scenario 2a		Scenario 2b	
	Photons	%	Photons	%	Photons	%	Photons	%
A	37,687	100	39,083	100	18,146	100	16,750	100
B	15,360	40.8	23,040	59.0	7,680	42.3	6,144	36.7
C	1,271	3.4	8,896	22.8	3,813	21.0	5,083	30.3
D	400	1.0	2,558	6.5	233	1.3	592	3.5

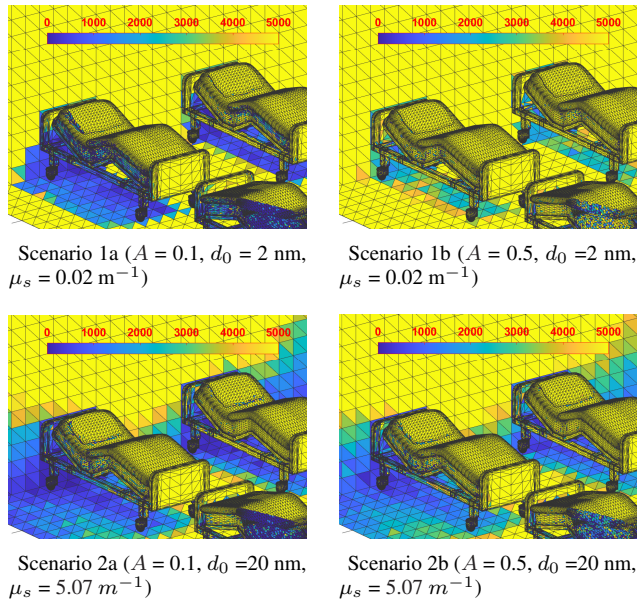


FIGURE 18. The UV exposure in each triangle zoomed in beds.

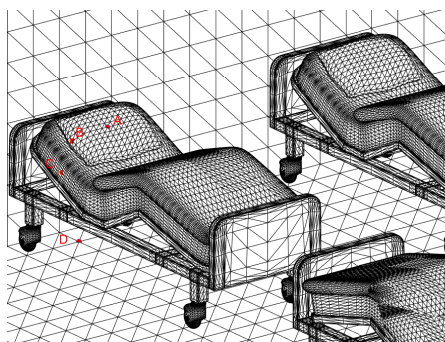


FIGURE 19. The position of the selected points A, B, C and D, used in Table V.

communications (affecting channel attenuation) and surface disinfection applications. Note that scenario 1b corresponds to natural conditions with slightly reduced visibility. It does not require increased droplet concentration, or large droplet diameter, which would necessitate nebulizers.

3) Mean total path length

Figure 20 illustrates the mean total path length, \bar{L} , of the photons absorbed in each triangle using a common color scale for comparison. In scenario 1a, \bar{L} is smaller than in

scenario 1b due to the increased surface albedo of the latter, which creates a significant number of surface reflections. On the other hand, in scenarios 2a and 2b, the \bar{L} value of the photons attenuated at each triangle increases compared to 1a and 1b due to the larger μ_s value. Moreover, the \bar{L} value for triangles close to the sources is smaller than that of more distant triangles, as expected. In all four scenarios and triangles, \bar{L} is greater in an empty room than in the furnished one. That can be attributed to the much greater number of triangles in the latter case causing more surface reflections and the higher probability of photon absorption having traveled smaller total paths.

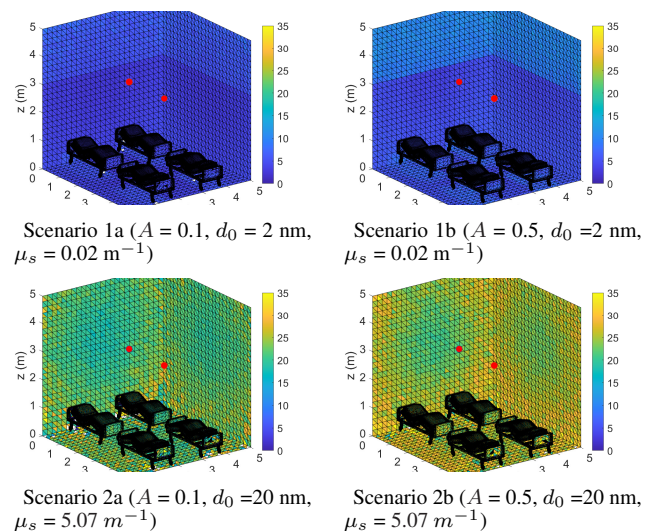


FIGURE 20. The mean total path length \bar{L} of the photons that ended up in each triangle.

V. CONCLUDING REMARKS

The UV-C light utilization for NLOS outdoor communications and disinfection of air or surfaces is already known to the scientific community. However, there seems to be a lack of computational modeling and simulation studies for indoor surface disinfection and NLOS communications. Furthermore, the emergence of epidemiological issues (such as the recent coronavirus crisis) and the appearance of studies indicating that specific far UV-C wavelengths may be safely used for the above purposes even in humans' presence [1], [12], raises the priority of these research issues to a great extent.

Our work focuses on covering that need mentioned above. More precisely, LaUV is based on an MC simulation of light propagation in the presence of any number of triangulated objects. The simulator considers scattering from air molecules and spherical water aerosols and droplets for any wavelength and utilizes the proper Rayleigh and Mie phase functions instead of the more popular approximations. Furthermore, the atmospheric composition can be parameterized by the temperature, the relevant humidity, and the concentration and distribution of water particle diameters. To our knowledge, no studies cover these areas with adequate physical accuracy and this level of parameterization.

Interestingly, LaUV applies to indoor setups, considering rooms of typical dimensions, empty or with furniture after triangulation. The measurable quantities on every triangle focus on the UV exposure, the distribution of ToA of photons, and the identification of the most prevalent phenomenon. These measurements allow for the design and prediction of UV applications to surface disinfection, as well as optical communications. Our initial results reveal subtle differences in the UV exposure patterns, both in LOS close to wall edges and corners and in NLOS, further affected by the presence of furniture. In addition, the effects of surface albedo and scattering coefficient, which also depends on the atmospheric conditions, further complicates the exposure prediction.

Of note, LaUV is very well suited for surface disinfection studies with well-defined geometric setups if combined with experimental survival curves of specific viruses, bacteria, or fungi. In addition, the output of the proposed system can readily be utilized for telecommunication channel modeling, both indoor and outdoor, considering almost any scenarios of geometric setup and atmospheric conditions. The simulator can be used to predict exposure with different geometries and assess the effect of environmental conditions. Initial results show that high albedo surfaces can increase exposure at hard-to-reach points, even with small values of μ_s , for small diameters of humidity droplets that are found under common atmospheric conditions, eliminating the need for nebulizers. Finally, despite the generally accepted concept that UV-C should not be used in human presence, newer results support the suitability of specific wavelengths with strong germicidal properties and less harmful effects on humans. This concept could also be explored using the proposed system, with 3D human models, appropriate source positioning, and optimal atmospheric conditions. Our future work will wade into these topics.

REFERENCES

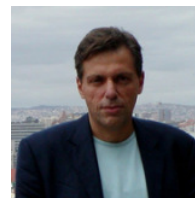
- [1] M. Buonanno, D. Welch, I. Shuryak, and D. J. Brenner, "Far-UVC light (222 nm) efficiently and safely inactivates airborne human coronaviruses," *Sci. Rep.*, vol. 10, 2020, article no:10285.
- [2] A. Vavoulas, H. Sandalidis, and D. Varoutas, "Node isolation probability for serial ultraviolet UV-C multi-hop networks," *IEEE J. Opt. Commun. Netw.*, vol. 3, no. 9, pp. 750–757, Sep. 2011.
- [3] S. Arya and Y. H. Chung, "Novel indoor ultraviolet wireless communication: Design implementation, channel modeling, and challenges," *IEEE Syst. J.*, vol. 15, no. 2, pp. 2349–2360, Jun. 2021.
- [4] A. Vavoulas, H. G. Sandalidis, N. D. Chatzidiamantis, Z. Xu, and G. K. Karagiannidis, "A survey on ultraviolet C-band (UV-C) communications," *IEEE Commun. Surveys Tuts.*, vol. 21, no. 3, pp. 2111–2133, 3rd Quart. 2019.
- [5] C. Xu and H. Zhang, "Channel analyses over wide optical spectra for long-range scattering communication," *IEEE Commun. Lett.*, vol. 19, no. 2, pp. 187–190, Feb. 2015.
- [6] H. Ding, G. Chen, A. K. Majumdar, B. M. Sadler, and Z. Xu, "Modeling of non-line-of-sight ultraviolet scattering channels for communication," *IEEE J. Sel. Areas Commun.*, vol. 27, no. 9, pp. 1535–1544, Dec. 2009.
- [7] Q. Zhang, X. Zhang, L. Wang, G. Shi, Q. Fu, and T. Liu, "Performance modeling of ultraviolet atmospheric scattering of different light sources based on Monte Carlo method," *Appl. Sci.*, vol. 10, no. 10, 2020, article no: 3564.
- [8] J. Colombi and K. Louedec, "Monte Carlo simulation of light scattering in the atmosphere and effect of atmospheric aerosols on the point spread function," *J. Opt. Soc. Am. A*, vol. 30, no. 11, pp. 2244–2252, Nov 2013.
- [9] T. Y. Aung, S. Arya, and Y. H. Chung, "A dynamic beamforming technique for ultraviolet-based indoor communications," *IEEE Sensors J.*, vol. 20, no. 18, pp. 10 547–10 553, Sep. 2020.
- [10] O. Haddad, M.-A. Khalighi, S. Zvanovec, and M. Adel, "Channel characterization and modeling for optical wireless body-area networks," *IEEE Open J. Commun. Soc.*, vol. 1, pp. 760–776, 2020.
- [11] W. Kowalski, *Ultraviolet Germicidal Irradiation Handbook*. Berlin, Germany: Springer-Verlag, 2009.
- [12] M. Buonanno, B. Ponnaiya, D. Welch, M. Stanislauskas, G. Randers-Pehrson, L. Smilenov, F. D. Lowy, D. M. Owens, and D. J. Brenner, "Germicidal efficacy and mammalian skin safety of 222-nm UV light," *Radiat. Res.*, vol. 187, no. 4, pp. 483–491, 2017.
- [13] H. Kitagawa, T. Nomura, T. Nazmul, K. Omori, N. Shigemoto, T. Sakaguchi, and H. Ohge, "Effectiveness of 222-nm ultraviolet light on disinfecting SARS-CoV-2 surface contamination," *Am. J. Infect. Control*, vol. 49, no. 3, pp. 299–301, 2021.
- [14] M. Heßling, K. Hönes, P. Vatter, and C. Lingensfelder, "Ultraviolet irradiation doses for coronavirus inactivation-review and analysis of coronavirus photoinactivation studies," *GMS Hyg. Infect. Control*, vol. 15, 2020, article no: Doc08.
- [15] "Ultraviolet air and surface treatment," in *2019 ASHRAE Handbook-HVAC Applications*, H. Kennedy, Ed., Atlanta, GA, USA, 2019.
- [16] K. C. Jelden, S. G. Gibbs, P. W. Smith, A. L. Hewlett, P. C. Iwen, K. K. Schmid, and J. J. Lowe, "Comparison of hospital room surface disinfection using a novel ultraviolet germicidal irradiation (UVGI) generator," *J. Occup Environ Hyg.*, vol. 13, no. 9, pp. 690–698, Sep. 2016.
- [17] B. Casini, B. Tuvo, M. L. Cristina, A. M. Spagnolo, M. Totaro, A. Baggiani, and G. P. Privitera, "Evaluation of an ultraviolet C (UVC) light-emitting device for disinfection of high touch surfaces in hospital critical areas," *Int. J. Environ. Res. Public Health*, vol. 16, no. 19, 2019, article no: 3572.
- [18] B. M. Tande, T. A. Pringle, W. A. Rutala, M. F. Gergen, and D. J. Weber, "Understanding the effect of ultraviolet light intensity on disinfection performance through the use of ultraviolet measurements and simulation," *Infect. Control Hosp. Epidemiol.*, vol. 39, no. 9, pp. 1122–1124, 2018.
- [19] N. R. A. R. Ropathy, H. L. Choo, C. H. Yeong, and Y. H. Wong, "UVC light simulation for room disinfection system," *MATEC Web Conf.*, vol. 335, 2021, article no: 03012.
- [20] Y. Cao, W. Chen, M. Li, B. Xu, J. Fan, and G. Zhang, "Simulation based design of deep ultraviolet LED array module used in virus disinfection," in *2020 21st International Conference on Electronic Packaging Technology (ICEPT)*, Guangzhou, China, 12–15 Aug. 2020.
- [21] "DIALux software," Accessed May 10, 2021. [Online]. Available: <https://www.dialux.com/en-GB/>
- [22] A. Baluja, J. Arines, R. Vilanova, J. Cortiñas, C. Bao-Varela, and M. T. Flores-Arias, "UV light dosage distribution over irregular respirator surfaces. methods and implications for safety," *J. Occup Environ Hyg.*, vol. 17, no. 9, pp. 390–397, Sep. 2020.
- [23] J. Arines, "Suitability of DIALux for designing UVC disinfection cabins," *Appl. Opt.*, vol. 60, no. 7, pp. 1821–1826, Mar 2021.
- [24] "Zemax OpticStudio," Accessed May 10, 2021. [Online]. Available: <https://www.zemax.com/products/opticstudio>
- [25] B. Gélébart, E. Tinet, J. M. Tualle, and S. Avriplier, "Phase function simulation in tissue phantoms: a fractal approach," *Pure Appl. Opt.: J. Eur. Opt. Soc. Part A*, vol. 5, no. 4, pp. 377–388, Jul. 1996.
- [26] R. Watté, B. Aernouts, R. V. Beers, E. Herremans, Q. T. Ho, P. Verboven, B. Nicolai, and W. Saeys, "Modeling the propagation of light in realistic

- tissue structures with MMC-fpf: a meshed Monte Carlo method with free phase function,” *Opt. Express*, vol. 23, no. 13, pp. 17467–17486, Jun 2015.
- [27] A. N. Yaroslavsky, I. V. Yaroslavsky, T. Goldbach, and H.-J. Schwarzmaier, “Influence of the scattering phase function approximation on the optical properties of blood determined from the integrating sphere measurements,” *J. Biomed. Opt.*, vol. 4, no. 1, pp. 47–53, 1999.
- [28] C. Zhu and Q. Liu, “Review of monte carlo modeling of light transport in tissues,” *J. Biomed. Opt.*, vol. 18, no. 5, p. 050902, 2013.
- [29] Q. Fang, “Mesh-based monte carlo method using fast ray-tracing in plücker coordinates,” *Biomed. Opt. Express*, vol. 1, no. 1, pp. 165–175, 2010.
- [30] H. Shen and G. Wang, “A tetrahedron-based inhomogeneous monte carlo optical simulator,” *Phys. Med. Biol.*, vol. 55, no. 4, p. 947, 2010.
- [31] M. Quinten, *Optical Properties of Nanoparticle Systems: Mie and beyond*. Weinheim, Germany: John Wiley & Sons, Ltd, 2011.
- [32] A. Cox, A. J. DeWeerd, and J. Linden, “An experiment to measure Mie and Rayleigh total scattering cross sections,” *Am. J. Phys.*, vol. 70, no. 6, pp. 620–625, 2002.
- [33] J. R. Frisvad, “Importance sampling the Rayleigh phase function,” *J. Opt. Soc. Am. A*, vol. 28, no. 12, pp. 2436–2441, Dec 2011.
- [34] “Relative humidity,” *Hyperphysics*. Accessed May 10, 2021. [Online]. Available: <http://hyperphysics.phy-astr.gsu.edu/hbase/Kinetic/relhum.html>
- [35] M. F. Chaplin, “Structure and properties of water in its various states,” in *Encyclopedia of Water*, P. A. Maurice, Ed., vol. 1. Hoboken, NJ, USA: John Wiley & Sons, Ltd, 2019.
- [36] C. Tomasi and F. Tampieri, “Size distribution models of small water droplets in mist and their volume extinction coefficients at visible and infrared wavelengths,” *Atmos. Environ.*, vol. 10, no. 11, pp. 1005–1013, 1976.
- [37] “Refractiveindex.info,” Accessed May 10, 2021. [Online]. Available: <https://refractiveindex.info>
- [38] “Visibility,” *Wikipedia*. Accessed May 10, 2021. [Online]. Available: <https://en.wikipedia.org/wiki/Visibility>
- [39] G. M. Hale and M. R. Querry, “Optical constants of water in the 200-nm to 200- μ m wavelength region,” *Appl. Opt.*, vol. 12, no. 3, pp. 555–563, Mar 1973.
- [40] C. Rodes, T. Smith, R. Crouse, and G. Ramachandran, “Measurements of the size distribution of aerosols produced by ultrasonic humidification,” *Aerosol Sci. Tech.*, vol. 13, no. 2, pp. 220–229, 1990.
- [41] C. F. Bohren and D. R. Huffman, *Absorption and Scattering of Light by Small Particles*. Weinheim, Germany: John Wiley & Sons, Ltd, 1998.
- [42] M. Abramovitz and I. A. Stegun, *Handbook of Mathematical Functions with Formulas, Graphs, and Mathematical Tables*, 9th ed. New York, NY, USA: Dover (Publications, Inc.), 1972.
- [43] G. W. Petty and W. Huang, “The modified gamma size distribution applied to inhomogeneous and nonspherical particles: Key relationships and conversions,” *J. Atmos. Sci.*, vol. 68, pp. 1460–1473, 2011.
- [44] S. A. Prahl, “A Monte Carlo model of light propagation in tissue,” in *Dosimetry of laser radiation in medicine and biology*, vol. 10305. International Society for Optics and Photonics, 1989, article no: 1030509.
- [45] A. Mikš, P. Novák, and J. Novák, “Calculation of aberration and direction of a normal to aspherical surface,” *Opt. Laser Technol.*, vol. 45, pp. 708–712, 2013.
- [46] T. Möller and B. Trumbore, “Fast, minimum storage ray-triangle intersection,” *J. Graph. Tools*, vol. 2, no. 1, pp. 21–28, 1997.
- [47] J. Tuszynski, “Triangle/ray intersection,” Mathworks, May 10 2021. [Online]. Available: <https://de.mathworks.com/matlabcentral/fileexchange/33073-triangle-ray-intersection>
- [48] R. Chadysšiene and A. Girgždys, “Ultraviolet radiation albedo of natural surfaces,” *J. Environ. Eng. Landsc. Manag.*, vol. 16, no. 2, pp. 83–88, 2008.
- [49] J. Turner and A. V. Parisi, “Ultraviolet radiation albedo and reflectance in review: The influence to ultraviolet exposure in occupational settings,” *Int. J. Environ. Res. Public Health*, vol. 15, no. 7, 2018, article no: 1507.



tions.

MARIA S. BALTADOUROU graduated from the Dept. of Physics, University of Athens, Greece, and obtained her MSc in Informatics and Computing Biomedicine in the Dept. of Computer Science and Biomedical Informatics, University of Thessaly, Greece. She is currently a Ph.D. student at the Laboratory of Medical imaging in the Dept. of Computer Science and Biomedical Informatics, Univ. of Thessaly, Greece, working on light propagation issues in tissues with biomedical applica-



KONSTANTINOS K. DELIBASIS graduated from the Dept. of Physics, University of Athens, Greece, and obtained his MSc in Medical Physics and Ph.D., entitled “Genetic Algorithms in Medical Image Analysis” from the Dept. of Biomedical Physics and Bio-engineering, University of Aberdeen, UK. He is currently an Associate Professor at the Dept. of Computer Science and Biomedical Informatics, Univ. of Thessaly, Greece. His research interests include processing and analyzing biomedical signals, images, and video. He is the author of more than 50 journal papers, and he has taught more than ten different undergraduate and postgraduate courses.



GEORGIOS N. TSIGARIDAS graduated from the Dept. of Physics, University of Patras, Greece, and obtained his MSc and Ph.D. degrees in laser physics and nonlinear optics, respectively, from the same University. He is currently working as Assistant Professor at the Dept. of Physics, School of Applied Mathematical and Physical Sciences, National Technical University of Athens, Greece. His research interests include nonlinear optics, laser-matter interactions, photonic sensors, interactions of charged Dirac and Weyl particles with electromagnetic fields, etc. He is the author of more than 50 journal papers, and he has taught several undergraduate and postgraduate courses, mainly regarding general physics, laser physics, optoelectronics, etc.



HARILAOS G. SANDALIDIS was born in Florina, Greece, in 1972. He received a five-year Diploma degree in Electronics and Computer Engineering and an MSc degree in Business Administration at the Production Engineering and Management Dept. from the Technical University of Crete, Greece, in 1995 and 1998, respectively. He also received an MSc degree in Radiofrequency and Microwave Communications and a Ph.D. degree in the Telecommunications area at Electronics and Telecommunications (former Electronics and Electrical engineering) Dept. from the University of Bradford, UK, in 1996 and 2002, respectively. From 1996 to 2001, he was a research assistant at the Telecommunications Systems Institute of Crete, Greece, working towards his Ph.D. degree in collaboration with the University of Bradford. After his military service, he joined TEMAGON, the technology consulting branch of the Hellenic Telecommunications Organization (OTE Group), in 2002, where he was involved in the risk mitigation program for the 2004 Olympic Telecommunication Network in collaboration with Telcordia Technologies, Inc. He also worked as a senior investigator for the Greek Ombudsman Office. In March 2009, he joined the University of Central Greece as a Lecturer at the Dept. of Computer Science and Biomedical Informatics. He is now an Associate Professor at the same Dept., which currently belongs to the University of Thessaly. His significant research interest lies in optical wireless networking, including free-space optics, underwater optical networks, and visible light communications.



GEORGE K. KARAGIANNIDIS (M'96-SM'03-F'14) was born in Pithagorion, Samos Island, Greece. He received the University Diploma (5 years) and Ph.D. degree, both in electrical and computer engineering, from the University of Patras, in 1987 and 1999, respectively. From 2000 to 2004, he was a Senior Researcher at the Institute for Space Applications and Remote Sensing, National Observatory of Athens, Greece. In June 2004, he joined the faculty of the Aristotle University of Thessaloniki, Greece, where he is currently Professor in the Electrical & Computer Engineering Dept. and Head of Wireless Communications & Information Processing (WCIP) Group. He is also an Honorary Professor at South West Jiaotong University, Chengdu, China. His research interests are in the broad area of Digital Communications Systems and Signal processing, with emphasis on Wireless Communications, Optical Wireless Communications, Wireless Power Transfer, and Applications and Communications & Signal Processing for Biomedical Engineering. Dr. Karagiannidis has been involved as General Chair, Technical Program Chair, and member of Technical Program Committees in several IEEE and non-IEEE conferences. In the past, he was Editor in several IEEE journals, and from 2012 to 2015, he was the Editor-in-Chief of IEEE Communications Letters. Currently, he serves as Associate Editor-in-Chief of IEEE Open Journal of Communications Society. Dr. Karagiannidis is one of the highly cited authors across all areas of Electrical Engineering, recognized by Clarivate Analytics as a Web-of-Science Highly-Cited Researcher in the six consecutive years 2015-2020.

...